

Effective optical properties of supported silicon nanopillars at telecommunication wavelengths

V. Pérez-Chávez^a, I. Simonsen^{b,c}, A.A. Maradudin^d, S. Blaize^e, E.R. Méndez^{a,*}

^a División de Física Aplicada, Centro de Investigación Científica y de Educación Superior de Ensenada, Carretera Ensenada-Tijuana No. 3918, Ensenada B.C. 22860, Mexico

^b Department of Physics, NTNU Norwegian University of Science and Technology, NO-7491 Trondheim, Norway

^c Surface du Verre et Interfaces, UMR 125 CNRS/Saint-Gobain, F-93303 Aubervilliers, France

^d Department of Physics and Astronomy, University of California, Irvine, CA 92697, USA

^e Laboratoire de Nanotechnologie et d'Instrumentation Optique, Université de Technologie de Troyes, 12 rue Marie Curie, BP-2060, 10010 Troyes Cedex, France

ARTICLE INFO

Keywords:

Silicon photonics
Effective medium theory
Transformation optics
Optical metamaterials
High index dielectrics
Light scattering

ABSTRACT

We measure and calculate the optical response of a structure consisting of a square array of subwavelength silicon posts on a silicon substrate at telecommunication wavelengths. By the use of the reduced Rayleigh equations and the Fourier modal method (rigorous coupled wave analysis) we calculate the reflectivity of this structure illuminated from vacuum by normally incident light. The calculated reflectivities together with experimentally determined ones, are used to test the accuracy of effective medium theories of the optical properties of structured silicon surfaces, and to estimate the effective refractive index of such surfaces produced by a homogeneous layer model.

1. Introduction

It has been established that Maxwell's equations are form-invariant under geometrical transformations [1], and that the consequences of a given transformation can be interpreted in terms of modifications of the material properties involved. Thus, regions with homogeneous properties are transformed into regions whose permittivity and permeability are determined by the mathematical nature of the transformation. This property has given rise to the field of transformation optics [1], which is an emerging area of optics in which coordinate transformations are used to design structures with novel optical properties. Using such techniques, designs for cloaking [2–4], and other interesting devices [5–7] have been proposed.

The practical realization of such structures and devices is, however, quite challenging, as the media in transformed space are in general anisotropic and their electromagnetic properties are functions of position. Not surprisingly, transformation optics is usually associated with the field of optical metamaterials, which are artificial materials whose permittivity and permeability can attain values that are different from those of materials found in nature. The concept of a metamaterial is intimately related to the notion of an effective medium; it relies on the idea that when the inclusions or heterogeneities are much smaller than the wavelength, the wave propagates as in a homogeneous medium with some effective optical properties that depend on the

geometry and the filling fraction of the inclusions.

Silicon and Silicon on Insulator (SOI) wafers constitute interesting platforms for experimental tests of transformation optics concepts, and for the implementation of novel designs for silicon photonics. On the one hand, silicon is a well studied material that is transparent in the near infrared and can be structured using electron beam lithography and ion etching techniques. Silicon photonics has become increasingly popular due to its natural integration with fiber optics communication links, and SOI wafers are designed to facilitate the implementation of two-dimensional integrated circuits. Additionally, the 2D nature of the photonic circuits makes the use of conformal mapping techniques [2] appropriate in their design. Conformal mappings constitute a class of two-dimensional transformations that have proved useful in the past for solving diffraction problems [8,9]. Implementing transformation optics concepts in silicon photonics is interesting from both, the conceptual and application points of view [10].

To our knowledge, however, the accuracy of the effective refractive index theories has not been tested for the kinds of structures and refractive index contrasts encountered in silicon photonics. In this paper, we explore this question for the case of silicon nanopillars over a silicon substrate. We test what are perhaps the simplest effective medium theories by comparing the measured reflectivity of fabricated samples with the results of calculations based on the Maxwell Garnett [11] and Bruggeman's [12] approaches, and through electromagnetic

* Corresponding author.

scattering calculations. We present calculations based on a numerical Rayleigh method that, although it has some limitation on the height of the pillars that can be dealt with, has the advantage of being computationally fast. The other method employed for the calculations is the rigorous coupled wave analysis (RCWA), also known as the Fourier modal method (FMM). The method is heavier computationally, but does not have the height limitations of the Rayleigh method. It is also better-suited for calculations with structures that have steep slopes.

The paper is organized as follows. The fabrication and characterization of the samples are described in Section 2. In Section 3, we present the expressions of the effective medium theories considered and the consequences of considering the structured layer as a homogeneous film for the calculation of the reflectivity. In Section 4 we briefly describe the two rigorous approaches to the calculation of the reflectivity that we have mentioned, namely the Rayleigh and the Fourier modal methods. The results are presented in Section 5, together with a discussion and, finally, in Section 6 we present our conclusions.

2. Nanostructured silicon samples

To explore the effective medium properties of nanostructured silicon layers at telecommunication wavelengths, we decided to focus on systems consisting of *circular* silicon nanopillars of a given radius that were arranged in an ordered or disordered fashion over the surface of the silicon substrate.

The fabrication of the samples started with 500 μm -thick, $1 \times 1 \text{ cm}^2$ substrates of bulk silicon. The substrates were cleaned by immersing them in an ultrasonic bath of acetone for 15 min. They were then rinsed in isopropanol, blow-dried under a nitrogen flux, baked on a hot plate at 300 $^\circ\text{C}$ for 15 min, and allowed to cool and stabilize overnight. The cleaned substrates were spin-coated with a primer layer of hexamethyldisilazane (HMDS), and a 200 nm layer of a negative electron resist (ma-N 2400). After baking them for two minutes at 80 $^\circ\text{C}$, the samples were coated with a layer of ESpacer 300Z, to prevent charging effects during the exposure. Then, the samples were rinsed with deionised water and dried.

The electron beam lithography (EBL) was carried out in a region of $1 \times 1 \text{ mm}^2$ using a Raith system with a dose of 26 $\mu\text{C}/\text{cm}^2$. To design the exposure pattern, we first generated a “geometry matrix”, consisting of ones and zeroes, that represents a top view of the desired geometry. The ones correspond to the silicon pillars and the zeroes to the region that will be etched at a later stage. The intended radius of the circular nanopillars was 75 nm. After exposure, all samples were developed in a solution made by combining equal quantities of ma-D 525 developer and deionised water for 60 s, rinsed in deionised water for another three minutes, and blow-dried under a nitrogen flux. Following the development, the samples were baked in an oven at 100 $^\circ\text{C}$ for ten minutes. An example of a periodic sample after the lithographic process is shown in Fig. 1(a). We point out that with negative resists, it is the exposed areas that remain on the surface of the substrate after development.

In the reactive ion etching (RIE) process, a plasma is generated by ionizing gas molecules in a low pressure chamber. The high-energy ions from the plasma attack the silicon on the wafer surface and remove material. To create the silicon pillars in our samples, the samples were subjected to a RIE process in a Plassys MEB400 using O_2 and SF_6 at 2×10^{-5} Torr and 90 W for three minutes in the first step, and O_2 with the same parameters for one minute in the second step. The height of the pillars is controlled by the time of etching. An example of the result is shown in Fig. 1(b).

Two types of samples were produced by this method. The first was a *periodic* structure, referred to as Sample A, in which the pillars formed a square lattice of period $a = 450 \text{ nm}$. In the second sample (Sample B), the pillars were placed in *random* positions with a pillar density that is

equal to that in the periodic sample. This was achieved by choosing the exposure area and the total number of pillars to have the same values that we have in the periodic sample; that is, the exposure area was $1 \times 1 \text{ mm}^2$ and the number of pillars was $M = (2222)^2$. The positions of the pillars were decided through the following procedure: The exposure area was divided into a square lattice of equally spaced intervals of the same size as the pillar diameter (which happens to be one-third of the period). Then, two uncorrelated random integers ξ_1 and ξ_2 were drawn from a uniform distribution on the interval $[1, N]$, where $N = 6666$ is the number of cells in each direction of the lattice. If the cell labeled (ξ_1, ξ_2) was not occupied and nor were its nearest neighbors, then a pillar was placed at the center of the cell (ξ_1, ξ_2) . This procedure was repeated until the number of pillars placed equaled M . Note that for samples produced in this way the minimum center-to-center separation between neighboring pillars is two pillar diameters (or 300 nm for the radius assumed here).

Figs. 1 and 2 present SEM images of Samples A and B, respectively. One observes that the fabricated nanopillars have a larger cross section area at the base than at the top [Fig. 1(b)]. By analyzing SEM images of Sample A, both those in Fig. 1 and other SEM images taken of the same sample, it was found that the pillars have a shape that can be approximated by a truncated cone with approximate top and base radii $\rho_t = 85 \pm 5 \text{ nm}$ and $\rho_b = 105 \pm 10 \text{ nm}$, respectively. The structure was measured to have a nominal period of $a = 450 \pm 5 \text{ nm}$. The height of the pillars was found to be $\zeta_0 = 190 \pm 5 \text{ nm}$. It should be mentioned that due to the discretization of the ideal positions, Sample A showed some undesired features; the distance between pillars ended up having periodic variations and the cross section of the pillars was not quite circular. These issues are illustrated in the SEM image presented in Fig. 1(a).

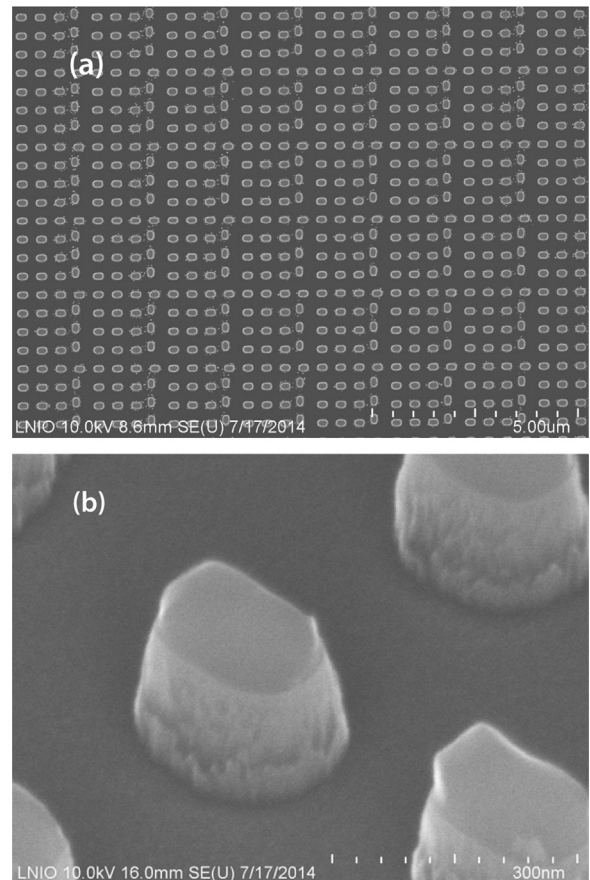


Fig. 1. SEM images of the periodic sample (Sample A) showing: (a) a large scale view of the structure after the lithography process but before etching; and (b) a detailed view of the nanopillars after etching.

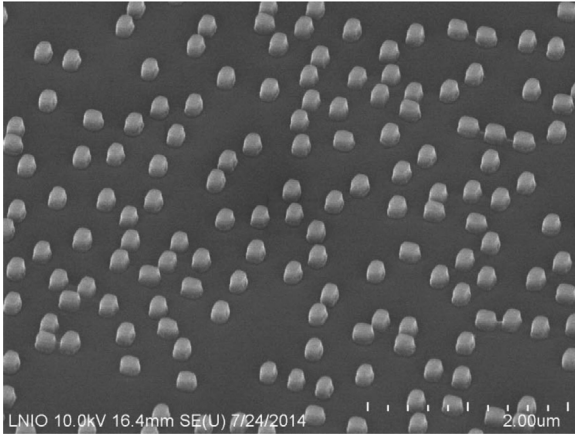


Fig. 2. SEM image of the random sample (Sample B) after etching.

For Sample B, the SEM images revealed that the top and base radii were, respectively, $\rho_t = 85 \pm 5 \text{ nm}$ and $\rho_b = 110 \pm 10 \text{ nm}$, while their height was found to be $\zeta_0 = 165 \pm 5 \text{ nm}$. The measured minimum distance between neighboring pillars was about 300 nm , which is in good agreement with the design parameters.

3. The reflectivity of the samples and effective medium theory

To measure the reflectivity, the samples were illuminated at near normal incidence [$\theta_0 \approx 2 \text{ mrad} \approx 1.15^\circ$] by a linearly polarized beam of light from a laser of wavelength $\lambda = 1.55 \mu\text{m}$ (Thorlabs LDM1550). A small angle of incidence was used to avoid the use of a beamsplitter in the measurements. The beam was focussed on the sample with a low power lens, and the reflected light was measured in the specular direction using a collecting lens and an InGaAs detector (Thorlabs DET20C). The contribution from the back surface of the sample was reduced by roughening it slightly and putting it in optical contact with an absorbing paste. Several readings of the optical power reflected from a given spot of the sample were averaged to obtain a measurement, that was later normalized by the signal produced by the flat areas of the sample (the reflectivity of these flat regions was in good agreement with that expected for a flat silicon surface). The estimated reflectivity values are shown in Table 1; the quoted values represent the mean and standard deviation calculated from ten measurements that correspond to different areas of the structured region of the samples. These measured reflectivities are significantly smaller than those obtained for a planar silicon substrate. Taking the value of the dielectric constant of silicon at the wavelength of the incident light to be $\epsilon = 12.25$, the Fresnel reflectivity for the planar silicon substrate is $R_0 \approx 0.3086$. Since the structures that we consider have lateral dimensions that are much smaller than the wavelength of the incident light, it is natural to assume that in this long wavelength limit, the layer containing the surface irregularities can be modeled as a homogeneous film of thickness $h = \zeta_0$ with an effective dielectric constant ϵ_{eff} [13]. The reflectivity of the system can then be calculated using the reflection coefficient of a layered system. For the case of a thin film over a substrate (three-media or three-layer system), one has [14].

Table 1

Reflectivity of the nanostructured silicon samples. The table summarizes the results of the measurements and the results expected on the basis of the EMTs. For a flat silicon surface, the reflectivity is expected to be $R_0 \approx 0.3086$.

Sample	Experimental	MG 2D	MG 3D	BR 2D	BR 3D
Periodic	0.2227 ± 0.0032	0.2596	0.2626	0.2514	0.2758
Non-periodic	0.2350 ± 0.0049	0.2717	0.2721	0.2631	0.2825

$$r = \frac{r_{12} + r_{23} \exp(2i\beta)}{1 + r_{12}r_{23} \exp(2i\beta)}, \quad (1)$$

where the subscripts 1, 2 and 3 refer to vacuum, the thin film, and the substrate, respectively; r_{ij} (with $i, j = 1, 2, 3$) represents the reflection amplitude of the interface between medium i and j ; and β denotes the optical path length for the light in the film. For the case of normal incidence, we can write

$$r_{ij} = \frac{n_i - n_j}{n_i + n_j}, \quad (2)$$

and

$$\beta = n_2 \frac{\omega}{c} h, \quad (3)$$

where $n_i = \sqrt{\epsilon_i}$ represents the refractive index of medium i . The reflectivity of the system is therefore given by

$$R = |r|^2 = \frac{r_{12}^2 + r_{23}^2 + 2r_{12}r_{23}\cos 2\beta}{1 + r_{12}^2r_{23}^2 + 2r_{12}r_{23}\cos 2\beta}. \quad (4)$$

The effective refractive index of the film, $\sqrt{\epsilon_{\text{eff}}}$, may then be estimated assuming a three-media model to invert reflectivity data obtained experimentally or through rigorous computer simulations. The result obtained in this way can be compared with estimations based on the effective medium theories, like the Maxwell Garnett theory, which has been used previously in the context of silicon photonics systems [10]. This permits the evaluation of the validity of effective medium theories for the estimation of the effective refractive index of a layer of supported silicon nanopyllars.

The Maxwell Garnett theory [11] relates the effective medium permittivity ϵ_{eff} , to the permittivities of the host (ϵ_1), the inclusions (ϵ_2) and the volume filling fraction f of the inclusions, which are assumed to be of a spherical shape and arranged in a cubic lattice. The mean distance between inclusions is assumed to be large enough to ensure that the Lorentz local field calculation is valid. The Maxwell Garnett formula takes the form [15].

$$\frac{\epsilon_{\text{eff}} - \epsilon_1}{\epsilon_{\text{eff}} + (d-1)\epsilon_1} = f \frac{\epsilon_2 - \epsilon_1}{\epsilon_2 + (d-1)\epsilon_1}, \quad (5)$$

where d represents the dimensionality of the problem ($d=3$ in the present case). The solution of Eq. (5) gives

$$\epsilon_{\text{eff}} = \epsilon_1 \frac{1 + (d-1)f\alpha}{1 - f\alpha}, \quad (6)$$

where $\alpha = (\epsilon_2 - \epsilon_1)/[\epsilon_2 + (d-1)\epsilon_1]$.

For the samples that we study the host medium is air, which has a permittivity $\epsilon_1 = 1$, and the inclusions are silicon, for which $\epsilon_2 = 12.25$. The filling fraction, defined as the ratio of the volume of inclusion to the volume of host material, was found to be $f=0.14$ using the parameters given in Section 2. To calculate the filling fraction for Sample A, we considered a unit cell of sides a , the period of our structures, with an embedded truncated cone of base radius ρ_b and top radius ρ_t . The volume filling fraction is then given by the ratio of the volume of the truncated cone to the volume of the cell. Since the average density of the pillars is the same in the two samples, the filling fraction of Sample B is the same as the filling fraction of Sample A. With these values Eq. (6) predicts that the effective medium should have a dielectric constant $\epsilon_{\text{eff}} = 1.40$. Using this value of ϵ_{eff} , and assuming that the wavelength of the incident light is $\lambda = 1.55 \mu\text{m}$, we have estimated the reflectivities of Samples A and B on the basis of Eq. (4). These values are given in Table 1, and are considerably larger than those obtained experimentally.

Alternatively, taking a 2D approach, one can view the system as a host of dielectric constant ϵ_1 that contains cylindrical inclusions of dielectric constant ϵ_2 . This can represent, for instance cylindrical silicon posts in air. For the case of normal incidence, the polarization

is perpendicular to the axes of the cylinders (transverse electric excitation, or p polarization), and the 2D Maxwell Garnett approach yields expressions (5) and (6) with $d=2$ [15–17]. In this case, the calculated effective permittivity is $\epsilon_{\text{eff}} = 1.27$ for the same filling fraction of $f=0.14$. The estimated values of the reflectivity of Samples A and B are also presented in Table 1. Although these values are closer than those obtained with the 3D formula, they still differ from the experimental ones.

The Maxwell Garnett result is only valid in the dilute limit. As the filling factor increases, the difference between the host material and the inclusions becomes less clear and the theory is expected to fail. Motivated by the need for an effective medium approximation that treats the components in a symmetric fashion, Bruggeman developed the approach that today bears his name [12,13]. It also has the advantage that it can straightforwardly be generalized to more than two components. For a two-component system, Bruggeman's approach yields the following expression [15,18].

$$(1-f) \left(\frac{\epsilon_1 - \epsilon_{\text{eff}}}{\epsilon_1 + (d-1)\epsilon_{\text{eff}}} \right) + f \left(\frac{\epsilon_2 - \epsilon_{\text{eff}}}{\epsilon_2 + (d-1)\epsilon_{\text{eff}}} \right) = 0. \quad (7)$$

This equation is quadratic in ϵ_{eff} and its (physically acceptable) solution is

$$\epsilon_{\text{eff}} = \frac{1}{2(d-1)} \left(\gamma + \sqrt{\gamma^2 + 4(d-1)\epsilon_1\epsilon_2} \right), \quad (8)$$

where $\gamma = d\bar{\epsilon} - \epsilon_1 - \epsilon_2$ and $\bar{\epsilon} = (1-f)\epsilon_1 + f\epsilon_2$. In writing Eqs. (7) and (8), we have assumed that, within the unit cell of sides a , the probability of having a material with dielectric constant ϵ_2 is f , and the probability of having material with ϵ_1 is $1-f$. In contrast with the model of Maxwell Garnett, the model of Bruggeman allows for an arbitrary concentration of the inclusions.

Under the 3D Bruggeman approach, the calculated effective permittivity is $\epsilon_{\text{eff}} = 1.17$ for the same filling fraction $f=0.14$ that we used with the Maxwell Garnett theory and, with the 2D approach, the effective permittivity is $\epsilon_{\text{eff}} = 1.30$. The reflectivities expected for Samples A and B on the basis of these values are shown in Table 1.

4. Rigorous theoretical approaches

In the preceding section we found that the reflectivity estimated for our structures by means of the effective medium theories (EMTs) did not agree with the one obtained experimentally. Thus, we turned to more accurate ways for calculating the reflectivity of our samples as a function of the heights of their pillars, namely the reduced Rayleigh equation (RRE) and the Fourier modal method (FMM). We now describe these approaches. The structures considered consist of pillars of silicon in a doubly periodic array on a silicon substrate in contact with air. The geometry is illustrated in Fig. 3.

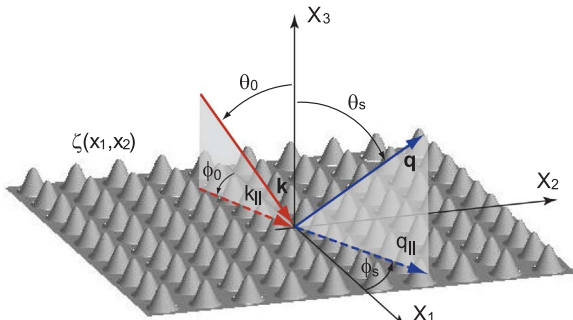


Fig. 3. Schematic diagram of the scattering geometry considered.

4.1. The reduced Rayleigh equation

The system we consider consists of vacuum in the region $x_3 > \zeta(\mathbf{x}_{\parallel})$ and a dielectric medium whose dielectric constant is ϵ in the region $x_3 < \zeta(\mathbf{x}_{\parallel})$. Here $\mathbf{x}_{\parallel} = (x_1, x_2, 0)$ is a position vector in the x_1x_2 plane. The surface profile function $\zeta(\mathbf{x}_{\parallel})$ is assumed to be a doubly periodic function of \mathbf{x}_{\parallel} , $\zeta(\mathbf{x}_{\parallel} + \mathbf{x}_{\parallel}(l)) = \zeta(\mathbf{x}_{\parallel})$, where $\mathbf{x}_{\parallel}(l)$ is a translation vector of a two-dimensional Bravais lattice

$$\mathbf{x}_{\parallel}(l) = l_1 \mathbf{a}_1 + l_2 \mathbf{a}_2. \quad (9)$$

Here $\mathbf{a}_1 = (a, 0)$ and $\mathbf{a}_2 = (0, a)$ are the two non collinear primitive translational vectors of the lattice, while l_1 and l_2 are any positive or negative integers, or zero, which we denote collectively by l . We also introduce the lattice reciprocal to the one defined by Eq. (9). Its lattice sites are given by

$$\mathbf{G}_{\parallel}(m) = m_1 \mathbf{b}_1 + m_2 \mathbf{b}_2, \quad (10)$$

where the primitive translation vectors of this lattice $\mathbf{b}_1 = \frac{2\pi}{a}(1, 0)$ and $\mathbf{b}_2 = \frac{2\pi}{a}(0, 1)$, are defined by the equation

$$\mathbf{a}_i \cdot \mathbf{b}_j = 2\pi\delta_{ij}, \quad i = 1, 2; \quad j = 1, 2, \quad (11)$$

where δ_{ij} is the Kronecker symbol. In Eq. (10) m_1 and m_2 are any positive or negative integers, or zero, which we denote collectively by m .

The surface is illuminated from the vacuum by a monochromatic plane wave of angular frequency ω . The total electric field in the region $x_3 > \zeta(\mathbf{x}_{\parallel})$ then consists of an incoming incident wave and a superposition of outgoing scattered waves,

$$\mathbf{E}(\mathbf{x}; t) = [\mathbf{E}^{(i)}(\mathbf{x}|\omega) + \mathbf{E}^{(s)}(\mathbf{x}|\omega)] \exp(-i\omega t), \quad (12a)$$

where $\mathbf{x} = (x_1, x_2, x_3)$ and the incident and scattered electric fields, respectively, can be written in the forms

$$\begin{aligned} \mathbf{E}^{(i)}(\mathbf{x}|\omega) = & \left\{ \frac{c}{\omega} [\alpha_0(k_{\parallel}, \omega) \hat{\mathbf{k}}_{\parallel} + k_{\parallel} \hat{\mathbf{x}}_3] E_{0p}(\mathbf{k}_{\parallel}) + (\hat{\mathbf{k}}_{\parallel} \times \hat{\mathbf{x}}_3) E_{0s}(\mathbf{k}_{\parallel}) \right\} \\ & \times \exp[i\mathbf{k}_{\parallel} \cdot \mathbf{x}_{\parallel} - i\alpha_0(k_{\parallel}, \omega)x_3], \end{aligned} \quad (12b)$$

and

$$\begin{aligned} \mathbf{E}^{(s)}(\mathbf{x}|\omega) = & \sum_{\mathbf{G}_{\parallel}} \left\{ \frac{c}{\omega} [-\hat{\mathbf{K}}_{\parallel} \alpha_0(K_{\parallel}, \omega) + \hat{\mathbf{x}}_3 K_{\parallel}] A_p(\mathbf{K}_{\parallel}) + (\hat{\mathbf{K}}_{\parallel} \times \hat{\mathbf{x}}_3) A_s(\mathbf{K}_{\parallel}) \right\} \\ & \times \exp[i\mathbf{K}_{\parallel} \cdot \mathbf{x}_{\parallel} + i\alpha_0(K_{\parallel}, \omega)x_3]. \end{aligned} \quad (12c)$$

In writing these expressions we have introduced the scattering amplitudes $A_p(\mathbf{K}_{\parallel})$ and $A_s(\mathbf{K}_{\parallel})$ and defined the functions

$$\mathbf{K}_{\parallel} = \mathbf{k}_{\parallel} + \mathbf{G}_{\parallel}, \quad (13)$$

and

$$\alpha_0(K_{\parallel}, \omega) = \left[\left(\frac{\omega}{c} \right)^2 - K_{\parallel}^2 \right]^{\frac{1}{2}}, \quad \text{Re } \alpha_0(K_{\parallel}, \omega) > 0, \quad \text{Im } \alpha_0(K_{\parallel}, \omega) > 0. \quad (14)$$

An expression similar to the one given by Eq. (12) can be written for the transmitted electric field $\mathbf{E}^{(t)}(\mathbf{x}|\omega)$ in the region $x_3 < \zeta(\mathbf{x}_{\parallel})$. However, it has been shown [19] that this field can be eliminated from the scattering problem, which greatly simplifies the derivation of the relations between the scattering amplitudes $A_{\alpha}(\mathbf{K}_{\parallel})$ and the amplitudes $\mathbf{E}_{0\beta}(\mathbf{k}_{\parallel})$ that define the incident field. We write this relation in the form ($\alpha = p, s, \beta = p, s$)

$$A_{\alpha}(\mathbf{K}_{\parallel}) = \sum_{\beta} \mathbf{R}_{\alpha\beta}(\mathbf{K}_{\parallel}|\mathbf{k}_{\parallel}) \mathbf{E}_{0\beta}(\mathbf{k}_{\parallel}). \quad (15)$$

The matrix $\mathbf{R}(\mathbf{K}_{\parallel}|\mathbf{k}_{\parallel})$ is found to be the solution of the matrix equation [19]

$$\begin{aligned} \sum_{\mathbf{G}_{\parallel}} \frac{\hat{I}(\alpha(\mathbf{K}_{\parallel}, \omega) - \alpha_0(\mathbf{K}_{\parallel}, \omega)) \mathbf{K}_{\parallel} - \mathbf{K}'_{\parallel}}{\alpha(\mathbf{K}_{\parallel}, \omega) - \alpha_0(\mathbf{K}'_{\parallel}, \omega)} \mathbf{M}^+(\mathbf{K}_{\parallel} \mathbf{K}'_{\parallel}) \mathbf{R}(\mathbf{K}'_{\parallel} \mathbf{k}_{\parallel}) \\ = - \frac{\hat{I}(\alpha(\mathbf{K}_{\parallel}, \omega) + \alpha_0(\mathbf{k}_{\parallel}, \omega)) \mathbf{K}_{\parallel} - \mathbf{k}_{\parallel}}{\alpha(\mathbf{K}_{\parallel}, \omega) + \alpha_0(\mathbf{k}_{\parallel}, \omega)} \mathbf{M}^-(\mathbf{K}_{\parallel} \mathbf{k}_{\parallel}), \end{aligned} \quad (16)$$

where

$$\hat{I}(\gamma | \mathbf{G}_{\parallel}) = \frac{1}{a_c} \int_{a_c} d^2 x_{\parallel} \exp(-i \mathbf{G}_{\parallel} \cdot \mathbf{x}_{\parallel}) \exp[-i \gamma \zeta(\mathbf{x}_{\parallel})] \quad (17)$$

$$\mathbf{R}(\mathbf{K}'_{\parallel} \mathbf{k}_{\parallel}) = \begin{bmatrix} R_{pp}(\mathbf{K}'_{\parallel} \mathbf{k}_{\parallel}) & R_{ps}(\mathbf{K}'_{\parallel} \mathbf{k}_{\parallel}) \\ R_{sp}(\mathbf{K}'_{\parallel} \mathbf{k}_{\parallel}) & R_{ss}(\mathbf{K}'_{\parallel} \mathbf{k}_{\parallel}) \end{bmatrix}, \quad (18)$$

and

$$\mathbf{M}^{\pm}(\mathbf{K}_{\parallel} \mathbf{K}'_{\parallel}) = \begin{bmatrix} M_{pp}^{\pm}(\mathbf{K}_{\parallel} \mathbf{K}'_{\parallel}) & M_{ps}^{\pm}(\mathbf{K}_{\parallel} \mathbf{K}'_{\parallel}) \\ M_{sp}^{\pm}(\mathbf{K}_{\parallel} \mathbf{K}'_{\parallel}) & M_{ss}^{\pm}(\mathbf{K}_{\parallel} \mathbf{K}'_{\parallel}) \end{bmatrix}, \quad (19)$$

with

$$M_{pp}^{\pm}(\mathbf{K}_{\parallel} \mathbf{K}'_{\parallel}) = K_{\parallel} K'_{\parallel} \pm \alpha(\mathbf{K}_{\parallel}, \omega) \hat{\mathbf{K}}_{\parallel} \cdot \hat{\mathbf{K}}'_{\parallel} \alpha_0(\mathbf{K}'_{\parallel}, \omega) \quad (20a)$$

$$M_{ps}^{\pm}(\mathbf{K}_{\parallel} \mathbf{K}'_{\parallel}) = -\left(\frac{\omega}{c}\right) \alpha(\mathbf{K}_{\parallel}, \omega) (\hat{\mathbf{K}}_{\parallel} \times \hat{\mathbf{K}}'_{\parallel})_3 \quad (20b)$$

$$M_{sp}^{\pm}(\mathbf{K}_{\parallel} \mathbf{K}'_{\parallel}) = \pm \left(\frac{\omega}{c}\right) (\hat{\mathbf{K}}_{\parallel} \times \hat{\mathbf{K}}'_{\parallel})_3 \alpha_0(\mathbf{K}'_{\parallel}, \omega) \quad (20c)$$

$$M_{ss}^{\pm}(\mathbf{K}_{\parallel} \mathbf{K}'_{\parallel}) = \left(\frac{\omega}{c}\right)^2 \hat{\mathbf{K}}_{\parallel} \cdot \hat{\mathbf{K}}'_{\parallel}. \quad (20d)$$

Here $a_c = |\mathbf{a}_1 \times \mathbf{a}_2|$ is the area of the primitive unit cell of the lattice defined by Eq. (9). In the numerical calculations to be carried out using the reduced Rayleigh equation, the surface profile function will be rotationally symmetric inside each unit cell, $\zeta(\mathbf{x}_{\parallel}) = \zeta(x_{\parallel})$. Therefore the angular integration in Eq. (17) will produce a J_0 -Bessel function and we are left with a one dimensional integration over the radial coordinate x_{\parallel} . If we assume that $\zeta(x_{\parallel}) = 0$ for $x_{\parallel} > R$, the integral (17) can be rewritten as

$$\begin{aligned} \hat{I}(\gamma | \mathbf{G}_{\parallel}) &= \delta_{\mathbf{G}_{\parallel} 0} + \frac{1}{a_c} \int_0^R dx_{\parallel} x_{\parallel} \int_{-\pi}^{\pi} d\phi [\exp(-i \gamma \zeta(x_{\parallel})) - 1] \times \exp(-i \mathbf{G}_{\parallel} x_{\parallel} \cos \phi) \\ &= \delta_{\mathbf{G}_{\parallel} 0} + \frac{2\pi}{a_c} \int_0^R dx_{\parallel} x_{\parallel} J_0(\mathbf{G}_{\parallel} x_{\parallel}) [\exp(-i \gamma \zeta(x_{\parallel})) - 1] \\ &= \delta_{\mathbf{G}_{\parallel} 0} + \frac{2\pi}{a_c} \sum_{n=1}^{\infty} \frac{(-i \gamma)^n}{n!} \int_0^R dx_{\parallel} x_{\parallel} J_0^n(\mathbf{G}_{\parallel} x_{\parallel}) \zeta^n(x_{\parallel}). \end{aligned} \quad (21)$$

The integrals inside the summation in this expression were calculated numerically.

In the present work we are primarily interested in the reflectivity of the surface. The reflectivity for light of polarization α is given by

$$R_{\alpha}(\theta_0, \phi_0) = |\mathbf{R}_{\alpha\alpha}(\mathbf{k}_{\parallel} \mathbf{k}_{\parallel})|^2, \quad (22)$$

where \mathbf{k}_{\parallel} is expressed in terms of the polar and azimuthal angles of incidence (θ_0, ϕ_0) by $\mathbf{k}_{\parallel} = (\omega/c) \sin \theta_0 (\cos \phi_0, \sin \phi_0, 0)$.

For the calculations presented in this work, we consider only cases in which the period $a \ll \lambda$. In such circumstances only the specular order is substantial (i.e. there is no diffraction). Moreover, in this initial evaluation, we consider only the case of normal incidence. Thus, the electric field is then always perpendicular to the axis of rotation of the posts.

4.2. The Fourier modal method

To model the reflectivity of the studied samples, we adapted the *Fourier modal method* (FMM) also known as the *rigorous coupled wave analysis* (RCWA) [20–22]. This (Fourier-space) simulation method assumes that the geometry is *periodic* and it is particularly well suited for the study of dielectric systems. It is also assumed that

the geometry is piecewise invariant in the vertical direction (the x_3 direction); if this is not the case, a staircase approximation is adopted so that a curved geometry is divided into a set of layers each of which is uniform in the vertical direction. The electromagnetic fields within each layer are expanded in Bloch waves (Floquet functions) so that the desired periodicity of the fields is guaranteed. The full electromagnetic field is obtained by satisfying the boundary conditions at each of the interfaces between the layers. In this way the Maxwell's equations are converted into an infinitely large set of algebraic equations. To be able to solve it on the computer, this set is truncated at a large but finite Fourier order. For additional details on the FMM method we refer the interested reader to Refs. [20–22].

The FMM is a highly accurate method for calculating the reflectivity of a periodic structure. However, there are several reasons why it may lead to poor performance. First, FMM computations involve solving eigenvalue systems, which are computationally expensive to solve. Second, when many layers are used to discretize a given geometry, boundary conditions must be enforced at the interfaces between layers, resulting in a large linear system [23].

Also, being a Fourier-space method it suffers several drawbacks. The main one is its slow convergence compared to other methods like the RRE method presented here. In the presence of materials with a high dielectric contrast, the Gibbs phenomenon [24] to which it gives rise is particularly severe. The same Gibbs phenomenon introduces ringing in the real space reconstruction of a function. The amplitude of the Gibbs ringing is a problem independent of the number of Fourier components.

In this work, we use the publicly available FMM code called S^4 (*Stanford Stratified Structure Solver*) [22], a frequency-domain computational electromagnetics tool that can compute reflection, transmission, or absorption spectra of periodic structures composed of layers invariant in the direction normal to the periodicity. The electromagnetic fields throughout the structure can also be obtained. The S^4 -package also provides a set of FMM formulations. This is beneficial since different formulations can have different convergence rates and therefore can produce better results in shorter amounts of computation time.

5. Results and discussion

In the calculations we considered two circularly symmetric profile forms for the supported silicon posts. The first one consists of *truncated cones* characterized by their top and base radii ρ_t and ρ_b (see Fig. 4), and defined mathematically by

$$\zeta(x_{\parallel}) = \begin{cases} \zeta_0 & 0 \leq x_{\parallel} < \rho_t \\ \zeta_0 \frac{\rho_b - x_{\parallel}}{\rho_b - \rho_t} & \rho_t \leq x_{\parallel} < \rho_b, \\ 0 & \rho_b \leq x_{\parallel} \end{cases} \quad (23)$$

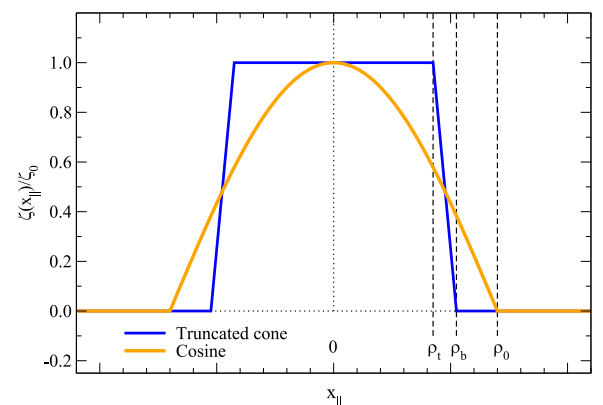


Fig. 4. The truncated cone and cosine forms assumed for the pillars in the modeling.

where $0 \leq \rho_t \leq \rho_b$ and $\zeta_0 \geq 0$. The model is simple but fairly realistic, as attested by the electron microscope images presented in Fig. 1(a). The values used in the calculations for the base and top radii were the experimentally determined ones, namely, $\rho_t = 85 \text{ nm}$ and $\rho_b = 105 \text{ nm}$. For the pillar heights ζ_0 achieved experimentally the surface slopes can be quite large, and this poses a problem for the method based on the Rayleigh hypothesis.

To circumvent this problem in the calculations based on the RRE, we considered profiles in the form of a *cosine*, defined mathematically as (see Fig. 4)

$$\zeta(x_{\parallel}) = \begin{cases} \zeta_0 \cos\left(\frac{\pi x_{\parallel}}{2\rho_0}\right) & 0 < x_{\parallel} < \rho_0, \\ 0 & x_{\parallel} > \rho_0 \end{cases} \quad (24)$$

where $\zeta_0 > 0$ is the height and $\rho_0 > 0$ is the half-width at the base of the particle. The base radius of the cosine profile was chosen in such a way that, for the same height, its volume is the same as that of the truncated cone. With our experimental parameters, this resulted in a value of $\rho_0 = 140 \text{ nm}$. It is important to point out that, although a cosine does not represent a good fit to the experimental shape of the pillars, the adoption of this shape does not change the volume fraction of the inclusions in the structured region and permits calculations based on the RRE with larger height values.

Fig. 5 presents FMM calculated results for the reflectivity $R(\zeta_0)$ (solid lines) of the truncated cones as a function of their height ζ_0 obtained using the S^4 -software package [22]. The truncated cones of circular cross-section were characterized by a top radius $\rho_t = 85 \text{ nm}$, a base radius $\rho_b = 105 \text{ nm}$ and height ζ_0 . The period of the square lattice was $a = 450 \text{ nm}$, and we assumed normally incident illumination with linearly polarized light of wavelength $\lambda = 1550 \text{ nm}$. At this wavelength the dielectric constant of silicon is $\epsilon = 12.25$. In obtaining these results $N = 600$ in-plane Fourier components were retained in the calculations (the number of reciprocal lattice vectors inside a circular domain), and the height of the truncated cones, ζ_0 , was divided into $L = 10$ layers of equal thickness. It was found that increasing N and L above these values did not result in any noticeable change in the simulation results; at least, this was the case for the geometrical parameters that we considered. The radius of the disc approximating the cone inside each layer was taken as the cone's radius at the center-height of the layer.

We observe, in Fig. 5, that the FMM calculated reflectivity values agree rather well with the reflectivity values measured for Samples A and B (red filled circles in Fig. 5). Moreover, the values of the geometrical parameters assumed in performing the FMM calculations are in good agreement with the values of the corresponding geometrical parameters obtained by analyzing the SEM images of the samples [Figs. 1 and 2].

It is particularly interesting to note that the FMM simulated and measured reflectivity values agree equally well for Samples A and B. It is recalled that Sample A is periodic, which is what is assumed in FMM calculations, while Sample B is random but with the same (surface) density of nanopillars as for Sample A. The fact that the results of the FMM calculations also agree well for Sample B we take as an indication that it is the density of pillars that is the key parameter in determining the reflectivity of the sample, at least, this is the case for the wavelength that was assumed in performing the measurements and calculations. It is speculated that this agreement will no longer hold true when the wavelength is reduced so that more than one diffraction channel is open.

The FMM formulation termed Polarization Basis (or “Pol”) in Ref. [22], was used in performing the FMM calculations reported in Fig. 5. This formulation is original to the code S^4 , and it gave the fastest convergence, at least, for the geometrical parameters that we assumed. Some of the other FMM formulations available in S^4 (and other FMM software packages) converged more slowly; this we attribute to the high value of the dielectric constant of silicon ($\epsilon = 12.25$) [22].

An inspection of the SEM images of the structures [Fig. 1] seems to reveal that the cross section of the structures are elliptical instead of having the circular shape assumed in performing the above calculations. An elliptical cross section will lead to a difference in the reflectivity for an electric field oriented along the long or short axis of the ellipse even at normal incidence. To investigate what effect this elongated shape will have on the reflectivity, we took the two semi-axes of the base to be $(1.00 \pm 0.05)\rho_b$, and similarly for the top semi-axis $(1.00 \pm 0.05)\rho_t$. With these values the reflectivity of unpolarized light at normal incidence departed only a few percent from what was obtained for the reflectivity of the corresponding truncated cones of a circular cross section defined by the radii ρ_b and ρ_t (and the same height ζ_0).

The FMM calculations presented in Fig. 5 are computationally intensive. It is therefore of interest to explore alternative computational approaches and we will here use the RRE approach introduced in Section 4.1. In the first set of RRE calculations the truncated cones assumed in the FMM calculations were considered. The results of such calculations are presented in Fig. 5 as filled blue triangles. Here the error bars indicate $\pm |1 - R_a - T_a|$ where T_a denotes the transmissivity for incident light of polarization a (see Refs. [25,26]). From Fig. 5 it is observed that the results of the FMM and RRE calculations agree rather well. However, from the inset to Fig. 5 it is apparent that the RRE results for the truncated cones of height $\zeta_0 > 60 \text{ nm}$ can not be trusted due to the lack of energy conservation. It is speculated that the poorer convergence property seen for the RRE approach when applied to the truncated cone is due to the steep slopes and the sharp corners around the top radius ρ_t [27]. Therefore, the next set of calculations were performed with the RRE approach for pillars of a cosine form characterized by a base radius $\rho_0 = 140 \text{ nm}$. As we have mentioned, this radius was chosen so that the volumes of the cosine particles and the truncate cones are the same for structures of the same height. The reflectivity values calculated by the RRE method for the cosine profile are presented in Fig. 5 as filled orange diamonds. For comparison we also performed calculations of the reflectivity by the FMM for the same profile, and the results were found to agree well with what was obtained by the RRE approach [dashed orange line in Fig. 5]. Such good agreement hints towards the correctness of the obtained results. The deviation between the RRE and FMM calculated reflectivities for a

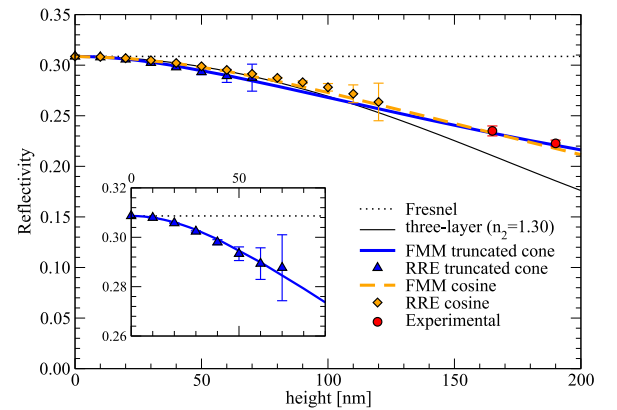


Fig. 5. The reflectivity $R(\zeta_0)$ as function of the height ζ_0 of the truncated cones or cosine shaped silicon particles supported by a planar silicon substrate. The particles formed a square lattice of period $a = 450 \text{ nm}$ and the structures were illuminated at normal incidence by p- or s-polarized light of wavelength $\lambda = 1550 \text{ nm}$. At this wavelength the dielectric constant of silicon is 12.25. The horizontal dotted lines indicate the Fresnel reflectivity of the corresponding planar silicon surface. The calculations of the reflectivity values were performed by the FMM and the solution of the RRE. The truncated cones were characterized by the height ζ_0 and top and base radii of $\rho_t = 85 \text{ nm}$ and $\rho_b = 105 \text{ nm}$, respectively. The radius of the cosine shaped particle was assumed to be $\rho_0 = 140 \text{ nm}$ so that its volume is the same as for the truncated cone of the same height. The thin solid black line represents the reflectivity of a three-layer model, Eq. (4), that fits the RRE (and FMM) simulation results in the low-height limit. The layer assumed in this model was characterized by the thickness ζ_0 and refractive index $n_2 = 1.30$.

cosine form is less than two percent at height $\zeta_0 = 100$ nm.

The reflectivity values obtained by the FMM and RRE approaches are observed to be slightly larger for the cosine form than those obtained for the truncated cones of the same volume. The fact that the reflectivity values are so similar for the two particle forms we take as an indication that the particle volume is one of the critical parameters for determining the reflectivity of the surface.

It should be mentioned that the computational time required to produce the FMM and RRE simulation results presented in Fig. 5 are rather different. For instance to check for convergence, we performed FMM calculations with $N=1000$ which took several days on a modern powerful desktop computer when it was run in sequential mode. Reflectivity calculations for the same particle form using the RRE approach required only a few seconds on the same computer. Even if this latter approach is not able to handle the largest pillar heights, it is still useful due to its much better computational performance.

On the basis of the low-height RRE simulation results for the cosine form presented in Fig. 5, the three-layer model (4) of thickness ζ_0 was fitted for the refractive index n_2 of the layer. In this way we obtained the effective refractive index $n_2 = 1.30$ for the layer. The corresponding dependence of the reflectivity with the height ζ_0 of the layer that is predicted by Eq. (4) is presented in Fig. 5 as a thin black line. These results demonstrate that a three-layer model of a fixed value of n_2 is inadequate to accurately describe the reflectivity variations predicted by the solution of the RRE and the FMM. The three-layer model reflectivity drops off too fast and for larger heights of the pillars the discrepancy is significant.

Fig. 6 presents the results for $R(\zeta_0)$ calculated from the Maxwell Garnett (blue lines) and Bruggeman effective medium theories (orange lines). The filled/open symbols in this figure represent the 2D/3D versions of these EMTs. It is observed from Fig. 6 that all the reflectivities obtained from the EMTs are significantly higher than those obtained from FMM (or RRE) simulations or the values measured for Samples A and B. The 2D versions of the considered EMTs produce results that are the closest to the simulation results, and the 2D Bruggeman result is better than the results obtained on the basis of the 2D Maxwell Garnett EMT (for the 3D EMTs it is the opposite). Even if the numerical values predicted by the EMTs depart substantially from the measured (and simulated) values, it is still noted that the slopes of the reflectivity curves $R(\zeta_0)$ are more realistic for the EMTs than for the three-layer model.

On the basis of the results presented in Fig. 6 it is concluded that both the (2D and 3D) Maxwell Garnett and Bruggeman EMTs fail to accurately predict the reflectivity of the silicon system under study. The

reason that the EMTs fail to predict the reflectivity we speculate is due to the high value of the dielectric constant of silicon. For instance, we have found that if the silicon substrate and pillars were instead made from glass ($\epsilon = 2.25$), then the 2D Maxwell Garnett and 2D Bruggeman EMTs produce virtually identical reflectivity values that deviate from the FMM calculated reflectivity by 0.5%, or less, over the entire interval $0 \leq \zeta_0 \leq 200$ nm of pillar heights.

6. Summary and conclusions

We have presented experimental results for the reflectivity of two specially prepared silicon samples at telecommunication wavelengths. The samples were fabricated by selectively etching silicon wafers to create structured surfaces that consists of subwavelength silicon pillars with a truncated-cone shape, over an otherwise flat silicon substrate. Using effective medium concepts, we have tried to model the structured region as a flat homogeneous layer over a flat silicon substrate. However, our attempts to reproduce the experimental measurements of the reflectivity using simple EMTs and this three-layer model have failed. The EMTs we have considered are the 2D (cylindrical inclusions) and 3D (spherical inclusions) versions of the Maxwell Garnett theory, as well as the Bruggeman approach.

Given the failure of the EMTs to model the physical situation, we have carried out more rigorous numerical calculations based on the FMM and the RRE. The former is often employed to model periodic structures in nanophotonics, while the latter is typically applied to rough surface scattering problems. The two numerical approaches produce results that are in good agreement with each other and with the experimental results. The FMM is computationally intensive, while the Rayleigh method is faster but cannot deal with surfaces that have large slopes. Although with this approach we were unable to reach the pillar heights of our samples, the method can be useful when the concept of a homogeneous layer is valid, as in that case the effective refractive index of the layer does not depend on the height of the pillars.

The rigorous results based on the FMM for the reflectivity as a function of pillar height indicate that it is not possible to model the problem as a three-media system and that the structured layer needs to be modeled as an inhomogeneous layer. We believe that the failure of the EMTs and the three-layer media model to describe adequately the physical situation is due to the large dielectric contrast between silicon and air. This idea is supported by the good numerical agreement we have found for similar structures made in glass, rather than silicon.

Acknowledgments

I. Simonsen acknowledges Dr. E. Garcia Caurel for fruitful and stimulation discussions on topics related to this work. V. Pérez-Chávez and E. R. Méndez are grateful for the support of CONACYT, under grant 180654. The research of I. Simonsen was supported in part by The Research Council of Norway Contract No. 216699; and The French National Research Agency (ANR) (ANR-15-CHIN-0003-01).

References

- [1] U. Leonhardt, T. Philbin, *Geometry and Light: The Science of Invisibility*, Dover Publications, Inc, Mineola, New York, 2010.
- [2] U. Leonhardt, Optical conformal mapping, *Science* 312 (2006) 1777–1780.
- [3] J.B. Pendry, D. Schurig, D.R. Smith, Controlling electromagnetic fields, *Science* 312 (2006) 1780–1782.
- [4] J. Li, J.B. Pendry, Hiding under the carpet: a new strategy for cloaking, *Phys. Rev. Lett.* 101 (2008) 203901.
- [5] M. Rahm, D. Schurig, D.A. Roberts, S.A. Cummer, D.R. Smith, J.B. Pendry, Design of electromagnetic cloaks and concentrators using form-invariant coordinate transformations of Maxwell's equations, *Photon. Nanostr.* 6 (2008) 87–95.
- [6] M.M. Sadeghi, S. Li, L. Xu, B. Hou, H.Y. Chen, Transformation optics with Fabry-Pérot resonances, *Sci. Rep.* 5 (2015) 8680.
- [7] A. Aubry, D.Y. Lei, A.I. Fernandez-Dominguez, Y. Sonnefraud, S.A. Maier, J.B. Pendry, Plasmonic light-harvesting devices over the whole visible spectrum,

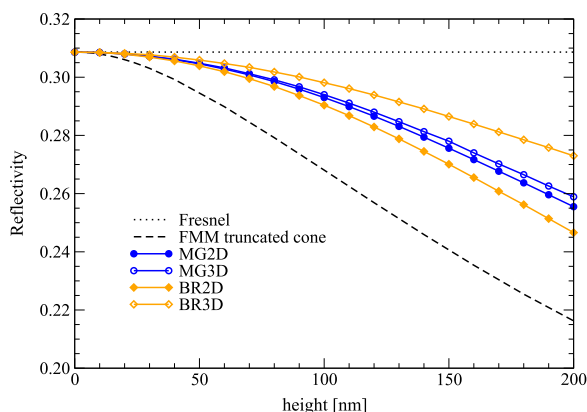


Fig. 6. The same as Fig. 5 but now the 2D and 3D Maxwell Garnett (MG) and Bruggeman (BR) effective medium theories are used to calculate the reflectivity at normal incidence for pillars of a given height. For comparison the FMM calculated and Fresnel reflectivities are given. Note that the since the truncated cone and the cosine bump both have the same volume, the filling fractions are the same for both particle forms. Therefore, the EMT reflectivities are identical for these two particle forms.

- Nano Lett. 10 (2010) 2574–2579.
- [8] M. Nevrière, M. Cadilhac, R. Petit, Applications of conformal mappings to the diffraction of electromagnetic waves by a grating, *IEEE Trans. Antennas Propag.* AP-21 (1973) 37–46.
 - [9] R.A. Depine, J.M. Simón, Diffraction grating efficiencies: conformal mapping method for a good real conductor, *Opt. Acta* 29 (1982) 1459–1473.
 - [10] L.H. Gabrielli, M. Lipson, Transformation optics on a silicon platform, *J. Opt.* 13 (2011) 024010.
 - [11] J.C. Maxwell Garnett, Colours in metal glasses and in metallic films, *Philos. T. Roy. Soc. A* 203 (1904) 385–420.
 - [12] D.A.G. Bruggeman, Dielektrizitätskonstanten und Leitfähigkeiten der Mischkörper aus Isotropen Substanzen, *Ann. Phys.* 416 (1935) 636–664.
 - [13] T.C. Choy, *Effective Medium Theory: Principles and Applications*, Oxford University Press, 1999.
 - [14] M. Born, E. Wolf, *Principles of Optics*, 4th ed., Pergamon Press, London, 1970.
 - [15] D.J. Bergman, The dielectric constant of a composite material – a problem in classical physics, *Phys. Rep.* 43 (1978) 377–407.
 - [16] Y. Wu, J. Li, Z.Q. Zhang, C.T. Chan, Effective medium theory for magnetodielectric composites: beyond the long-wavelength limit, *Phys. Rev. B* 74 (2006) 085111.
 - [17] A. Kirchner, K. Busch, C.M. Soukoulis, Transport properties of random arrays of dielectric cylinders, *Phys. Rev. B* 57 (1998) 277–288.
 - [18] D. Zhang, *Inverse Electromagnetic Problem for Microstructured Media*, University of Utah, 2007.
 - [19] N.E. Glass, A.A. Maradudin, V. Celli, Theory of surface-polariton resonances and field enhancements in light scattering from bigratings, *J. Opt. Soc. Am.* 73 (1983) 1240–1248.
 - [20] M.G. Moharam, Eric B. Grann, Drew A. Pommet, T.K. Gaylord, Formulation for stable and efficient implementation of the rigorous coupled-wave analysis of binary gratings, *J. Opt. Soc. Am. A* 12 (1995) 1068–1076.
 - [21] L. Li, Use of Fourier series in the analysis of discontinuous periodic structures, *J. Opt. Soc. Am. A* 13 (1996) 1870–1876.
 - [22] V. Liu, S. Fan, S4: a free electromagnetic solver for layered periodic structures, *Comput. Phys. Commun.* 183 (2012) 2233–2244.
 - [23] N.P. van der Aa, R.M.M. Mattheij, Computing shape parameter sensitivity of the field of one-dimensional surface-relief gratings by using an analytical approach based on RCWA, *J. Opt. Soc. Am. A* 9 (2007) 2692–2700.
 - [24] G. B. Arfken, H. J. Weber, *Mathematical Methods for Physicists*, 6th ed., Elsevier Academic Press, Burlington, MA, 2005, Section 14.5.
 - [25] A. Soubret, G. Berginc, C. Bourrelly, Application of reduced Rayleigh equations to electromagnetic wave scattering by two-dimensional randomly rough surfaces, *Phys. Rev. B* 63 (2001) 245411.
 - [26] Ø.S. Hetland, A.A. Maradudin, T. Nordam, P.A. Letnes, I. Simonsen, Numerical studies of the transmission of light through a two-dimensional randomly rough interface, *Phys. Rev. A* 95 (2017) 043808.
 - [27] J.-P. Banon and I. Simonsen, unpublished, 2016.